

First-Principles Calculations of Magnetite (Fe_3O_4) above the Verwey Temperature by Using Self-Consistent DFT + U + V

Nelson Naveas,* Ruth Pulido, Carlo Marini, Pierluigi Gargiani, Jacobo Hernandez-Montelongo, Ivan Brito, and Miguel Manso-Silván



Cite This: *J. Chem. Theory Comput.* 2023, 19, 8610–8623



Read Online

ACCESS |



Metrics & More

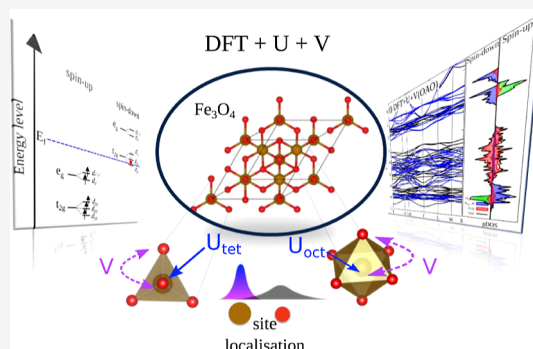


Article Recommendations



Supporting Information

ABSTRACT: In this report, we have used the DFT + U + V approach, an extension of the DFT + U approach that takes into account both on-site and intersite interactions, to simulate structural, magnetic, and electronic properties together with the Fe and O K-edge XAS spectra of Fe_3O_4 above the Verwey temperature (T_v). Moreover, we compared the simulated XAS spectra with experimental XAS data. We examined both orthogonalized and nonorthogonalized atomic orbital projectors and compared DFT + U + V to DFT, DFT + U , and HSE as a hybrid functional. It is noteworthy that, despite the widespread use of the same Hubbard U value for Fe_{oct} and Fe_{tet} at the DFT + U level in the literature, the HP code identified two distinct values for them using the Hubbard approaches (DFT + U and DFT + U + V). The resulting Hubbard U and V parameters are strongly dependent on the chosen orbital projectors. This study demonstrates how DFT + U + V can improve the structural, magnetic, and electronic properties of Fe_3O_4 compared to approximate DFT and DFT + U . In this context, DFT + U + V supports the half-metallic character of the bulk crystal Fe_3O_4 above T_v , since the Fermi level is found in the t_{2g} band with a Fe_{oct} down-spin. Thus, the observations in the current study emphasize the significance of intersite interactions in the theoretical analysis of Fe_3O_4 above the T_v .



1. INTRODUCTION

Despite being the preferred method for describing the electronic structure of condensed matter in materials science and engineering,^{1–3} approximate density functional theory (DFT) faces significant difficulties in adequately modeling the electronic structure and magnetic properties of transition-metal oxides, such as iron oxides.⁴ In part, this is due to the confined character of the Fe 3d orbitals and the substantial self-interaction error (SIE) of commonly used exchange–correlation functionals, including local density approximation (LDA) or generalized gradient approximation (GGA).^{5–7} To address SIE issues, a large number of studies employ hybrid DFT or DFT + U . On the one hand, hybrid DFT combines elements of both Hartree–Fock (HF) theory and approximate DFT functionals. Unfortunately, hybrid functionals are incredibly expensive compared to approximate DFT.^{8,9} On the other hand, in the DFT + U approach,^{10,11} an additional term is introduced into the approximate DFT energy functional, which describes the on-site Coulomb repulsion between electrons in localized d or f orbitals, while the remaining valence electrons are treated by the approximate DFT functionals. This term is derived from the simplified Hubbard model for strongly correlated electron systems and is typically denoted as U .¹² Although DFT + U combines increased accuracy with a low computational cost, it only

considers on-site interactions. As a result, it cannot adequately represent electronic hybridization in some materials because intersite interactions between an atom and its ligands are ignored. As a solution, the DFT + U + V method has been proposed as an extension, where V stands for intersite interactions. Thus, the DFT + U + V approach employs electronic interactions at both the on-site U and intersite V levels, adequately characterizing the intense intersite electronic hybridization in compounds made of transition metals.¹³ In the DFT + U + V method, a corrective term is added to the approximate DFT energy functional to improve the accuracy with which strongly correlated systems are described¹³

$$E_{\text{DFT}+U+V} = E_{\text{DFT}} + E_{U+V} \quad (1)$$

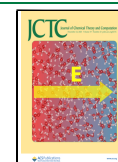
Here, the total energy of the system is composed of the E_{DFT} , which represents the approximate DFT energy, while E_{U+V} symbolizes the Hubbard term, that either incorporates the on-site U and intersite V Hubbard parameters. As in the

Received: August 7, 2023

Revised: October 10, 2023

Accepted: October 30, 2023

Published: November 17, 2023



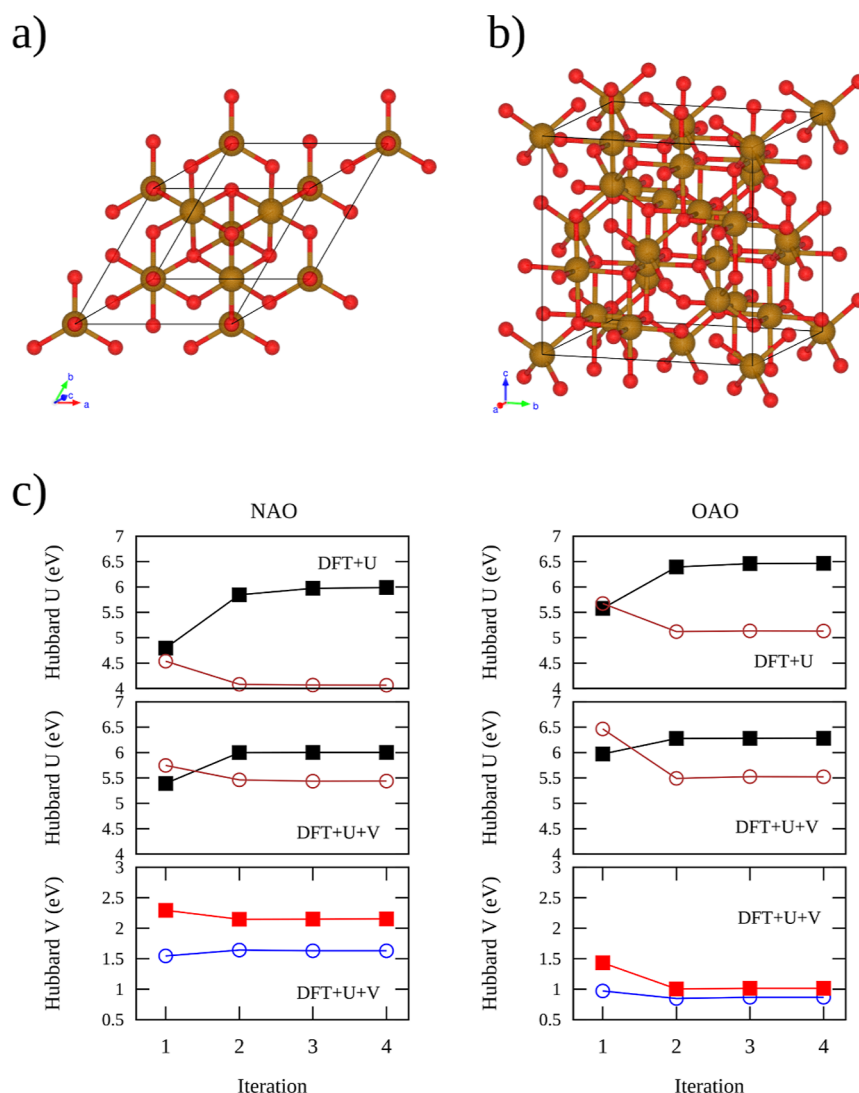


Figure 1. Crystal model of the (a) primitive and (b) unit cell of the Fe₃O₄. (c) Progression of Hubbard parameters (U and V) for bulk Fe₃O₄ behind each iteration of the self-consistent calculations for both DFT + U and DFT + U + V . Calculations were performed by using either NAO or OAO projectors. In the Hubbard U curves, the black and brown lines represent the Fe_{oct} and Fe_{tet} Hubbard U values, respectively. Similarly, the Hubbard V parameters associated with the shorter and longer Fe–O distances are represented by the red and blue lines in the Hubbard V curves.

simple DFT + U case, in DFT + U + V , the Hubbard U parameter represents the effective strength of the on-site Coulomb repulsion while the additional Hubbard parameter V explains how electrons interact effectively with neighboring sites, a crucial aspect for compounds that require orbital hybridization among different atoms. Inside the simple rotationally invariant model, the extended Hubbard term is expressed as follows

$$E_{U+V} = \frac{1}{2} \sum_I \sum_{\sigma m_1 m_2} U^I (\delta_{m_1 m_2} - n_{m_1 m_2}^{I\sigma}) n_{m_2 m_1}^{I\sigma} - \frac{1}{2} \sum_I \sum_{J(J \neq I)}^* \sum_{\sigma m_1 m_2} V^{IJ} n_{m_1 m_2}^{I\sigma} n_{m_2 m_1}^{J\sigma} \quad (2)$$

The atomic occupation matrices are determined by a generalized projection of the KS states onto the localized orbitals of neighboring atoms

$$n_{m_1 m_2}^{IJ\sigma} = \sum_k \sum_{\nu} \theta_{F, \nu k \sigma} \left\langle \psi_{\nu k \sigma}^o | \hat{P}_{m_2 m_1}^{IJ} | \psi_{\nu k \sigma} \right\rangle \quad (3)$$

Thus, both DFT + U and DFT + U + V are Hubbard-corrected DFT methods that improve accuracy while using less computing power than, for example, hybrid functionals. However, when these Hubbard-corrected DFT methods are used, the values of the Hubbard parameters are not known in advance. Calculating the Hubbard parameters from first-principles can be challenging as they are typically determined empirically or by fitting experimental data.^{14–17} However, there are several computational methods designed to calculate Hubbard parameters, such as the constrained DFT (cDFT) approach,^{18–25} Hartree–Fock-based approaches,^{26–31} the constrained random phase approximation (cRPA),^{32–37} a linear-response formulation of cDFT, and even a machine learning-based approach,¹⁶ among others. Nevertheless, there are some problems with these methods, such as the need to use supercells and expensive computing power. In order to overcome these issues, by using the density-functional

perturbation theory (DFPT) framework, Timrov has recently updated the Hubbard U linear response calculation.³⁸ Instead of using finite differences across supercell calculations, this method uses summing over monochromatic (wave-vector-specific) perturbations in primitive cells, making it more computationally efficient than the prior method. Moreover, the numerical stability and convergence are improved, and the computing process is simplified via enhanced automation. Also, via this formulation, it is possible to compute the intersite V parameters.³⁹

In this report, we used DFT + U + V to investigate magnetite (Fe_3O_4) above the Verwey temperature (T_v) and compared it to approximate DFT, DFT + U , along with a hybrid functional (HSE). Magnetite is an attractive and complex magnetic material with unique electronic and magnetic properties, making it a topic of intense interest in basic and applied research. It exhibits a notable phase transition at a specific temperature called the Verwey temperature (near $T_v \approx 120$ K), accompanied by a first-order metal–insulator behavior transition.⁴⁰ Although numerous aspects of the Verwey transition in bulk magnetite crystals have been researched since Verwey's seminal paper in 1939⁴¹ (especially below T_v), there is still an intense debate considering if this material presents a semiconductor or half-metallic nature above the T_v . In fact, it has been an important question whether the disordered charge, orbital, and trimeron correlations persist in the high-temperature cubic phase.⁴² In the present paper, we hypothesized that applying the DFT + U + V theory to investigate magnetite above the Verwey temperature transition can lead to a more accurate understanding of the material properties by considering both the on-site and intersite electronic correlation effects that are significant in this material. Our research focuses on the room-temperature cubic phase as this is where the semiconductor or semimetallic debate arises as well as being relevant to environmental and biomedical applications. Therefore, we first computed the on-site U and intersite V Hubbard parameters self-consistently from first principles using density functional perturbation theory (DFPT). Second, the Fe_3O_4 structure was optimized using the converged U and V Hubbard parameters. Finally, we examine the structural, magnetic, and electronic characteristics of Fe_3O_4 above the Verwey temperature transition using DFT + U + V .

2. METHODS

2.1. DFT Calculation Details. DFT calculations were computed with the Quantum Espresso computational package⁴³ using the plane-wave (PW) pseudopotential approach. In our study, we used both PBEsol and PBE pseudopotentials downloaded from the SSSP Precision Library v1.2.⁴⁴ In all calculations, the ferrimagnetic properties of Fe_3O_4 and the spin polarization were taken into account because of the strong antiferromagnetic interaction between the tetrahedral (Fe_{tet}) and octahedral (Fe_{oct}) Fe ions. Then, the spins of Fe_{oct} and Fe_{tet} were set up and down, respectively. The rhombohedral primitive cell (Figure 1a), which has 14 atoms, and the conventional unit cell (Figure 1b), which has 56 atoms, were both employed.

For the calculation of the Hubbard parameters, we used the HP code contained in Quantum Espresso.^{38,39,45} The HP code utilizes DFPT to calculate Hubbard parameters (on-site U and intersite V) within the context of DFT + U and DFT + U + V .⁴⁵ In DFPT calculations, we used the primitive cell with a

uniform Γ -centered k and q point mesh of $5 \times 5 \times 5$ and $2 \times 2 \times 2$ q point mesh, along with kinetic-energy cutoffs of 65 and 780 Ry for the wave function and the charge density, respectively. At this point, the self-consistent approach to compute U and V parameters was used, involving cyclic computations of the optimized structures and the subsequent recalculation of Hubbard parameters for each newly optimized crystal structure.³⁹

The BFGS quasi-Newton algorithm was used to optimize the crystal structures using the approximate DFT, DFT + U , and the extended DFT + U + V approaches. For total energy, forces, and pressure, we set convergence thresholds of 1×10^{-6} Ry, 1×10^{-5} Ry/Bohr, and 0.5 kbar, respectively. By applying a Hubbard U correction to Fe 3d states, DFT + U computations have been performed employing the simplified rotational-invariant formulation used by Cococcioni and de Gironcoli.⁴⁶ Also, utilizing the simplified version of Leiria Campo and Cococcioni,¹³ the intersite interaction among the Fe 3d and O 2p orbitals was corrected employing the Hubbard V parameter in DFT + U + V calculations. Nonorthogonalized atomic orbitals (NAOs) and orthogonalized atomic orbitals (OAOs) have been applied for the DFT + U and DFT + U + V computations.³⁹ We used the Marzari–Vanderbilt (MV) smearing technique⁴⁷ with a 1×10^{-2} Ry broadening parameter.

A uniform Γ -centered k point mesh of $10 \times 10 \times 10$ was used to calculate structural optimizations, band gaps, magnetic moments, and the projected and total density of states (DOS). At this level, kinetic-energy cutoffs of 90 and 1080 Ry were used for the wave function and the charge density, respectively. The magnetic moment per site for Fe atoms, which we outline in our paper, is obtained from the SCF calculations. This moment is equivalent to a weighted integration of the electronic moment within a sphere surrounding the nucleus. To determine the charge of Fe and O ions in Fe_3O_4 , Bader charge analysis was performed.^{48–51}

2.2. Experimental and Simulated XAFS Details. We conducted X-ray absorption spectroscopy experiments while maintaining a vacuum environment at the CLÆSS beamline of the ALBA CELLS synchrotron in Spain. The K-edge of Fe (7124 eV) measurements were carried out in a continuous mode utilizing a double-crystal Si(311) monochromator. To ensure the accuracy of measurements, we checked the energy calibration of each collected spectrum by aligning the first derivative maximum (7112 eV) of the XAS reference spectrum of a Fe foil, which was acquired alongside the sample. The absorption data have been collected in the transmission mode utilizing three adequately gas-filled ionization chambers at this energy. All spectra within the XANES region were sampled with an energy resolution of 0.3 eV. The specifications have been handled in accordance with the standard procedure. Pre-edge background subtraction and XANES normalization were conducted using a linear polynomial fit for the pre-edge region and a cubic polynomial fit for the postedge region of the absorption spectrum. Spectra were also separated based on the absorption jump. The processing of data was conducted utilizing ATHENA software, which is included in the IFEFFIT suite.

XAS measurements in the soft X-rays have been performed at beamlines BL29-BOREAS at the ALBA synchrotron (Spain). The synchrotron radiation emitted by a pure permanent magnet helical undulator (capable of delivering both linearly and circularly/elliptically polarized light) is first

intercepted by a plane and toroidal mirrors and then by the monochromator. This latter one is based on variable line spacing plane gratings, working at a fixed included angle of 175 or 177° in combination with dedicated spherical mirrors. Finally, two bendable mirrors arranged in Kirkpatrick–Baez geometry focus the beam on the sample. At the K-edge (543 eV), polarized XANES spectra were measured in total electron yield on sintered pieces. The incident X-ray flux measured as the TEY current on a clean gold mesh between the last optical element and the sample normalized the sample signal. All of the XANES spectra presented have been normalized. Initially, the linear pre-edge contribution is subtracted and then the jump is fixed to 1 at values well above the absorption edge. There has been no normalization or other unmentioned data manipulation.

By employing the Lanczos recursive procedure inside of the XSpectra code of Quantum Espresso distribution,^{52–54} simulations of Fe and O K-edge XANES spectra were carried out. In our calculations, the dipolar part of Fe and O K-edge XANES spectra was considered, neglecting both the quadrupole part and the core-hole in the final state. The convolution of the XANES spectra was produced employing a Lorentzian smearing arctangentlike function with an energy-dependent broadening.⁵⁵

The EXAFS signal of Fe₃O₄ has been extracted using the standard procedure previously reported.⁵⁶ Briefly, corresponding Fourier transforms have been conducted over the *k* range 2.6–14 Å^{−1} once it has been multiplied by *k*² in order to strengthen the signal in the higher *k*-region. The EXAFS oscillations have been modeled by utilizing the structures achieved through relaxation within DFT, DFT + *U*, and DFT + *U* + *V*. The FEFF-6 code⁵⁷ was used to calculate the theoretical amplitudes and phases of the various paths used in the analysis. The ARTEMIS program of the DEMETER suite⁵⁸ was then used to adapt the theoretical values to the experimental data (in *R* space).

3. RESULTS AND DISCUSSION

3.1. Calculations of Hubbard Parameters. In the Fe₃O₄, the on-site *U* correction is essential for describing Fe 3d states and the intersite *V* parameter is anticipated to be effective for characterizing Fe 3d–O 2p hybridization. Hence, we have determined the Hubbard parameters (*U* and *V*) for Fe₃O₄ through the self-consistent calculation method proposed by Timrov et al., 2021.³⁹ Figure 1c shows the progression of the *U* and *V* Hubbard parameters for the Fe₃O₄, employing NAO or OAO orbital projectors after each iteration. Interestingly, despite the fact that the literature widely uses the same Hubbard *U* value for Fe_{oct} and Fe_{tet}, here the HP code identified, by considering the occupation matrix, two different values for them. Regardless of the Hubbard-corrected theory utilized, the progression of *U* values, illustrated in Figure 1c, displays divergent trends for both Fe_{oct} and Fe_{tet}. The values for Fe_{oct} increased, while those for Fe_{tet} decreased from the initial to the final iteration. In general, the self-consistent procedure results in higher converged *U* values for Fe_{oct} than Fe_{tet} for both DFT + *U* and DFT + *U* + *V*. On the one hand, when DFT + *U* corrections are applied, the converged values of *U* depend strongly on the projector used. We find that the Hubbard *U* values for both Fe_{oct} and Fe_{tet} are consistently higher when using the OAO projectors compared to the NAO projectors. On the other hand, if the corrections are a DFT + *U* + *V* level, the dependence of the *U* values on the projector

used is not as strong as with DFT + *U* (the difference between NAO and OAO values is reduced). On the contrary, the projector used has a significant effect on the converged values of *V*, resulting in higher values when using NAO projectors than OAO. Similarly to the determined *U* values obtained, here the HP code identified two different values for the *V* parameter, one corresponding to Fe_{oct}–O and the other to Fe_{tet}–O interaction.

In a previous study, linear response calculations using DFT + *U* theory revealed different self-consistent *U* values for Fe_{oct} (4.7 eV) and Fe_{tet} (4.3 eV).⁵⁹ These results are consistent with our research, where we detected distinct *U* values for both Fe_{oct} and Fe_{tet}, with Fe_{oct} showing a *U* value higher than Fe_{tet}. Nevertheless, in our study, we found a greater contrast between Fe_{oct} and Fe_{tet} *U* values using DFPT. Differences in pseudopotential types and exchange–correlation functionals employed can account for the divergences between our outcomes and those of prior research.^{45,60,61} Additionally, our research emphasizes the significance of precisely determining the Hubbard *U* parameter and orbital projector selection, as well as the consideration of intersite interactions through the application of DFT + *U* + *V* theory.

The structural optimization involved in the self-consistent technique is essential to achieving the final Hubbard parameter values in Fe₃O₄ as previously described for hematite (α-Fe₂O₃),⁶² another widely used iron oxide. The importance of this process has also been demonstrated for other types of materials, such as SrTiO₃,⁶³ MnPO₄, LiMnPO₄,³⁹ and Fe-doped α-MnO₂.⁶⁴ The obtained Hubbard parameters after the fourth iteration are summarized in Table 1. The Hubbard

Table 1. Convergence Evolution of the Hubbard Parameters, *U* and *V*, Computed through DFPT for the Bulk Crystal Cell of Fe₃O₄

method	manifold	Hubbard <i>U</i> (eV)		Hubbard <i>V</i> (eV)	
		Fe _{oct} /Fe _{tet}		Fe _{oct} –O/Fe _{tet} –O	
DFT + <i>U</i>	NAO	5.9877/4.0631			
DFT + <i>U</i> + <i>V</i>	NAO	6.0008/5.44		1.6295/2.1545	
DFT + <i>U</i>	OAO	6.4674/5.1323			
DFT + <i>U</i> + <i>V</i>	OAO	6.2825/5.5229		0.8661/1.0145	

parameters are sufficiently converged for the majority of postprocessing applications when they are within 0.01 eV for the DFT + *U* and DFT + *U* + *V* approaches after the subsequent iterations.

3.2. Calculation of Structural Parameters. After determining the Hubbard parameters, we compared the experimental lattice parameter (*a*) and the residual volume (*V*) of the conventional Fe₃O₄ unit cell with those predicted by the different theories applied in our study. Note that Fe₃O₄ has a cubic inverse spinel structure (space group *Fd3m*) at room temperature, and there are a number of eight formula units in its conventional unit cell, which include 24 Fe and 32 O atoms. In our investigation, the crystal structure of Fe₃O₄ was fully relaxed at the different studied theories (DFT, DFT + *U*, and DFT + *U* + *V*), preserving its cubic symmetry. Table 2 compares the experimental value with the optimized lattice parameter (*a*) and the volume (*V*) of the Fe₃O₄ unit cell as achieved by different theories. The standard DFT approach, as previously reported for Fe₃O₄, subestimates the lattice parameter (1.47%) and the residual volume (4.35%). Although the Hubbard-corrected DFT approaches (the simple DFT + *U*

Table 2. Structural Parameters of the Unit Cell of Bulk Fe_3O_4 Computed via DFT, DFT + U , and DFT + U + V Theories

Hubbard manifold	method	a (Å)	V (Å)
	Exp	8.396	591.858
	DFT	8.272	566.092
NAO	DFT + U	8.484	610.768
NAO	DFT + U + V	8.333	578.744
OAO	DFT + U	8.463	606.095
OAO	DFT + U + V	8.446	602.568

and the extended DFT + U + V) result in different tendencies, they enhance the match against the volume and the experimental lattice parameter a . According to the Hubbard-corrected method that was utilized, the discrepancy for the calculated and experimental values drops to a range of 0.8–1.05% for DFT + U and 0.6–0.7% for DFT + U + V . In fact, it has been extensively reported that the DFT + U method (containing just the on-site correction) has improved the description of the structural properties of Fe_3O_4 and other transition-metal oxides. However, the DFT + U + V approach has not received the same level of attention. Also noteworthy is the fact that the Hubbard projector type significantly affects the resultant lattice parameter achieved by DFT + U and DFT + U + V . For example, we observe that DFT + U overestimates the lattice parameters by 1.05% when NAO projectors are used. On the other hand, the lattice parameter by DFT + U + V is subestimated by just 0.74%. Therefore, the best match with experiments was then discovered for NAO projectors to be at the DFT + U + V level.

Figure 2a shows the optimized Fe–O bond lengths in the conventional unit cell of Fe_3O_4 computed by DFT, DFT + U , and DFT + U + V theories. Experimentally, two Fe–O bonds can be distinguished by looking at the bond lengths in the conventional unit cell by using neutron powder high-resolution diffraction,⁶⁵ one of which is shorter and measures around 1.8885 Å, while the other is longer and measures around 2.0582 Å. These two Fe–O bonds correspond to those formed by Fe_{tet} and Fe_{oct} , respectively. As occurred for the lattice parameter results, approximate DFT underestimates both Fe–O bonds. In this sense, all Hubbard-corrected theories improve the results of both Fe–O bonds. However, the simpler of the Hubbard-corrected theories, DFT + U -NAO, shows a different pattern for the Fe–O bond lengths. This theory results in several distances for Fe_{tet} –O and Fe_{oct} –O due to the loss of crystalline symmetry after the structural optimization process. Interestingly, the rest of the Hubbard-corrected theories show just two Fe–O bond lengths, where DFT + U + V better describes their distances.

3.3. Magnetic Properties and Charge Analysis. Fe_3O_4 has a magnetic moment of +4 μ_B per formula unit in the basic ferrimagnetic model, which is completely attributed to the $\text{Fe}_{\text{oct}}^{2+}$ cations. The $\text{Fe}_{\text{tet}}^{3+}$ and $\text{Fe}_{\text{oct}}^{3+}$ cations cancel one another out.⁶⁶ This supports the hypothesis of half-metallic conduction and compares favorably with the experimental measurement of 4.07 μ_B .⁶⁷ Figure 2b shows the magnetic moments on Fe atoms in Fe_3O_4 calculated by the different investigated theories. The experimental magnetic moment values for the Fe_{oct} and Fe_{tet} are 3.97⁶⁵ and 3.8–4.2 μ_B ,^{65,68} respectively, as shown by dashed lines in Figure 2b. The magnetic moments calculated by DFT are 3.328 and –3.066 μ_B for Fe_{oct} and Fe_{tet} , respectively, which are drastically smaller than the exper-

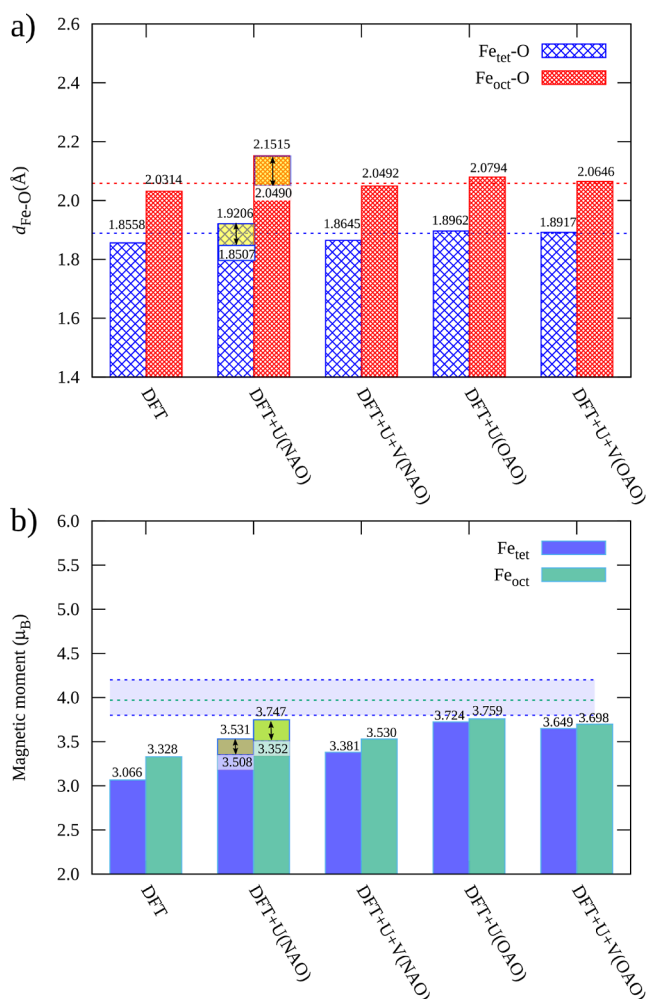


Figure 2. (a) Optimized Fe–O bond lengths and (b) Fe magnetic moment in the crystal cell of Fe_3O_4 calculated via DFT, DFT + U , and DFT + U + V theories. Dash lines correspond to the experimental data of Fe–O bonds and magnetic moments as appropriate.

imental values. Interestingly, the Hubbard corrections improve the estimation in all situations, although the results depend on the used theory as well as the used orbital projector. Additionally, they still underestimate the magnetic moment by 0.4–0.8 μ_B . Similar to the Fe–O distance result, DFT + U -NAO results in several magnetic moments for Fe_{oct} and Fe_{tet} because, under this theory, structural optimization causes a loss of symmetry. At the DFT + U level, the calculated magnetic moments for the Fe_{oct} and Fe_{tet} were 3.6792 and –3.5773 μ_B for NAO and 3.759 and –3.724 μ_B for the OAO projectors. When using DFT + U + V theory, the calculated magnetic moments for the Fe_{oct} and Fe_{tet} were 3.530 and –3.381 μ_B for NAO and 3.698 and –3.649 μ_B for the OAO projectors. Thus, the better agreement with the experimental results is DFT + U and DFT + U + V when using OAO projectors.

In order to determine the influence of the Hubbard correction theories on the Fe partial charges for the Fe_3O_4 , we performed a Bader charge analysis (Table S1). On the one hand, similarly to the Fe–O distances and magnetic moment results, DFT + U -NAO yields multiple charges for Fe_{oct} (3.438 e/3.621 e) and Fe_{tet} (3.654 e/3.681 e). On the other hand, at the DFT + U -NAO, DFT + U + V -NAO, and DFT + U + V -OAO levels, the charge coming from the Fe_{tet} and Fe_{oct} can be distinguished (Table S1). In addition to the Bader analysis, we

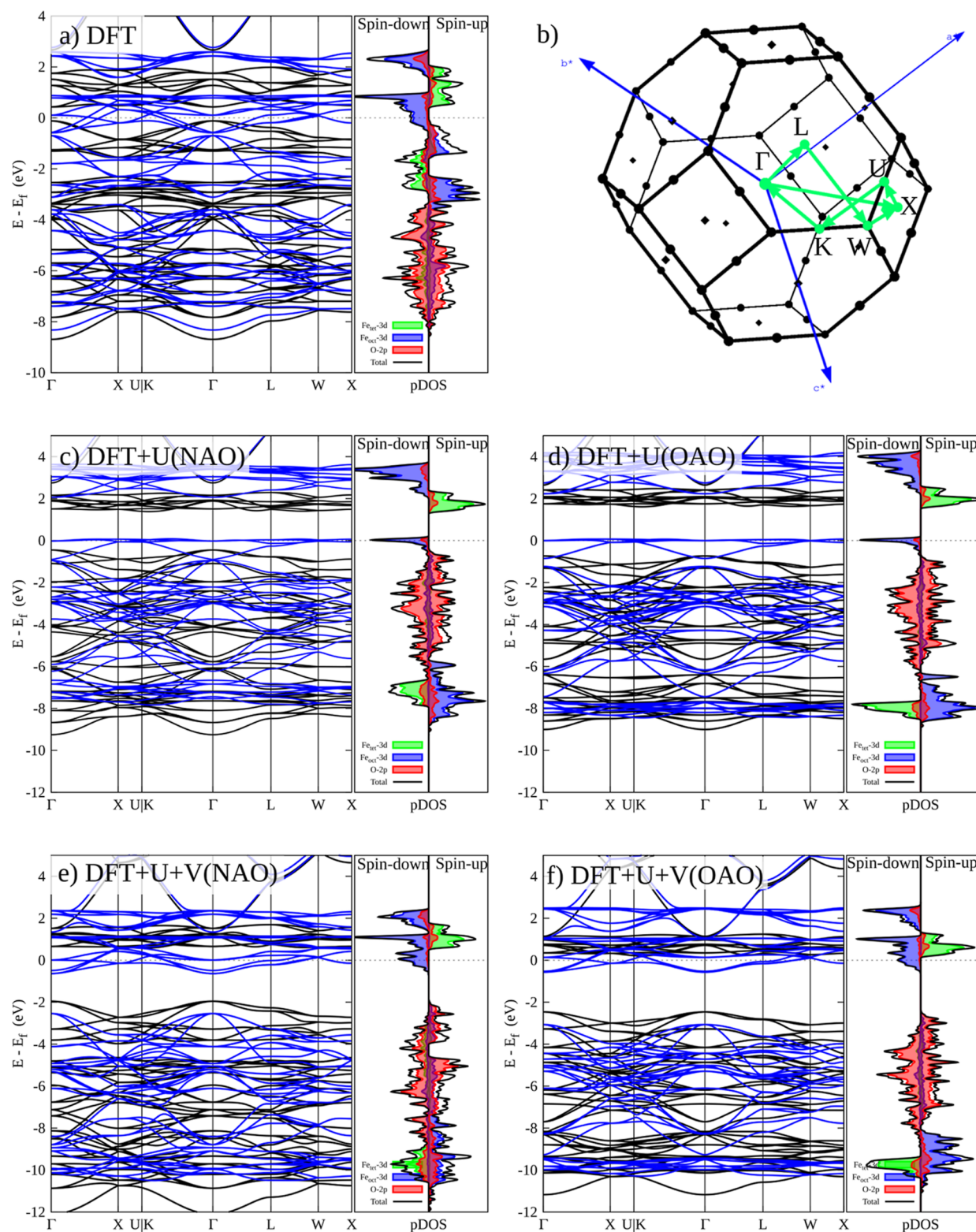


Figure 3. Band structures and pDOS for the Fe_3O_4 bulk crystal calculated by DFT (a), DFT + U (c,d for NAO and OAO, respectively), and DFT + U + V (e,f for NAO and OAO, respectively). The selected path in the reciprocal space is shown in (b).

have also carried out the method proposed by Sit et al. (2011)⁶⁹ to determine the oxidation states (OS) of Fe. This procedure involves separating the contributions of orbital mixing to the assigned charge from those due to the actual occupation of the d-orbitals. However, the application of this procedure to our system was challenging due to the presence

of multiple Fe sites. In fact, only DFT and U-NAO give multiple Fe OS values for Fe_{oct} (Fe^{2+} and Fe^{3+}). Nonetheless, of the 16 Fe_{oct} sites, only 4 are Fe^{2+} , indicating incomplete charge disproportionation. The remaining theories are unable to discriminate among Fe_{oct} of different OS, leading to an OS of Fe^{3+} for all sites (see Table S2).

3.4. Electronic Properties. The electronic structure of Fe_3O_4 has been studied using a wide variety of experimental approaches, such as angle-resolved photoelectron spectroscopy using synchrotron radiation,⁷⁰ optical-conductivity spectra,⁷¹ and photoemission spectroscopy,^{72,73} among others.

Figure 3 depicts the band structure and partial density of states (pDOS) of the Fe_3O_4 bulk crystal calculated through conventional DFT and different corrected Hubbard approaches by using NAO and OAO projectors. The band structure and the pDOS projected on the Fe_{oct} , Fe_{tet} , and O sites obtained by the DFT (Figure 3a) show that the Fe_3O_4 is a half-metallic oxide with a spin-up channel that displays semiconducting behavior and a spin-down channel that exhibits metallic behavior, which is in accordance with previous reports using LSDA⁷⁴ and PBE^{75,76} XC functionals. The spin-up band structure produced by the approximate DFT theory has an electronic structure with a direct band gap of 0.3 eV at the Γ point. In the vicinity of the Fermi energy, the pDOS indicates substantial hybridization of the O 2p and Fe 3d states. The conduction band is mostly made up of Fe 3d states, where the spin-up and down are composed of Fe_{tet} and Fe_{oct} respectively. This behavior is reversed in the valence band, where the spin-up is composed of Fe_{oct} and the spin-down of Fe_{tet} . Likewise, according to the pDOS, the O 2p states are localized in the valence band region between -3.0 and -8.0 eV. As a consequence of the SIE related to the approximate DFT, Fe 3d states are overdelocalized owing to their significant hybridization with O 2p states.

Figure 3c–f shows the band structure and pDOS of Fe_3O_4 by using corrected Hubbard approaches. At the DFT + U level, the result of the band structure and pDOS does not depend significantly on the orbital projector used (Figure 3c,d). Indeed, there are only small differences in the intensities of Fe states between DFT + U with NAO and OAO. On the one hand, the semiconducting nature of the electron spin-up of Fe_3O_4 is accurately described by the DFT + U theory, which results in a greater band gap (1.6 eV for NAO and 2.1 eV for OAO) than the approximate DFT. On the other hand, there exists a finite DOS at the Fermi energy in the spin-down channel. This is in line with previous results, where the electronic structure of Fe_3O_4 is described as half-metallic by using DFT + U theory. For both NAO and OAO projectors, the minimum of the conduction band is dominated by Fe 3d states, with Fe_{oct} at the spin-down channel and Fe_{tet} at the spin-up channel. Although the O 2p states dominate at the maximum of the valence band, finite and localized Fe_{oct} states persist, indicating the hybridized states in this area. Also, most of the Fe 3d states, which were originally close to the Fermi level in approximate DFT, have shifted to higher binding energy due to Coulomb interactions between Fe 3d electrons. The main difference in this region between the NAO and OAO projectors is that the OAO projector evidenced a colocalization between Fe_{oct} (spin-down) and Fe_{tet} (spin-up) at low energies around -8.0 eV. Interestingly, in contrast to approximate DFT theory, under the application of DFT + U , the O 2p states are localized at higher energies in the valence band region between -0.5 and -5.8 eV. The inclusion of the Hubbard V parameter through DFT + U + V calculations induces significant modifications to both the electronic structure of Fe_3O_4 (Figure 3e,f) in comparison to DFT + U . Despite the differences, DFT + U + V , like DFT + U , also supports the half-metallic nature of bulk crystal Fe_3O_4 above T_v , given that the Fermi level resides in a Fe_{oct} 3d down-spin

state. A major difference between DFT + U + V and DFT + U is that, in DFT + U + V , the down-spin Fe_{oct} 3d located at the Fermi energy exhibits a broader energy range. Another important difference is that DFT + U + V results in a greater band gap (2.3 eV for NAO and 2.4 eV for OAO) than the approximate DFT + U for the electron spin-up channel. Thus, DFT + U + V gets a better description of the semiconducting nature of the majority electron spin of Fe_3O_4 with a bigger band gap than DFT + U and a metallic behavior of the minority spin.

Figure 4 compares the conventional DFT employed in this work (PBEsol) with the HSE hybrid DFT functional to exhibit

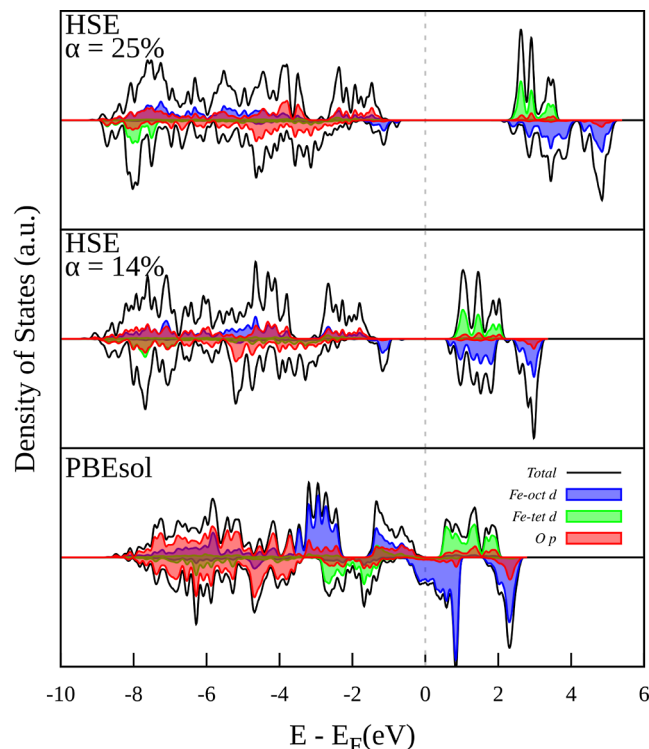


Figure 4. Comparison of the pDOS for the Fe_3O_4 bulk crystal calculated by DFT (PBEsol) and HSE hybrid functional at different exchange fractions ($\alpha = 14\%$ and $\alpha = 25\%$).

the total DOS and pDOS estimated for Fe_3O_4 . Here, to simulate the DOS and pDOS for the HSE functional, an SCF calculation was performed on the structure that had already been optimized using DFT + U + V -OAO. Different exchange fractions were used to demonstrate the necessity of refining this parameter in order to get a specific result. In fact, this indicates that using hybrid functionals is not a full first-principles method. Also, it is important to note that the utilization of hybrid functionals like HSE is considerably less efficient and more costly compared to approximate DFT and Hubbard-corrected DFT approaches. As shown in Figure 4, the HSE functional cannot describe the symmetrical charge distribution across Fe_{oct} atoms of the unit cell seen at room temperature, resulting in a semiconducting behavior for both spin channels. Due to charge order, which is also characterized by the distribution of magnetic moments among Fe_{oct} atoms and the emergence of a d–d optical band gap, symmetry breaking may lead to distortions of Fe_{oct} .⁷⁷ This result has been a topic of discussion for years.^{75–77} For example, Liu and Di Valentin, 2017⁷⁶ have demonstrated that using no-symmetry

restriction, DFT + U theory using a Hubbard $U = 3.5$ eV provokes opening a gap around the Fermi energy, thus causing a semiconducting behavior in the ground state of Fe_3O_4 . Our results do not show a semiconducting behavior, probably due to the lack of disproportionation of Fe states. However, when applying no-symmetry, the only theory used in this study that opens a complete gap around Fermi energy is DFT + U -NAO. In fact, in this case, the asymmetric ground state has a lower total energy than the symmetric state ($\Delta E = -0.47$ eV; Table S3). Neither DFT + U -OAO nor DFT + U + V theories open a gap when using the no-symmetry restriction (Figure S1). We have also performed calculations with DFT + U -OAO, DFT + U + V -NAO, and DFT + U + V -OAO theories starting from the symmetry-broken DFT + U -NAO structure to assess whether the charge order would arise spontaneously. However, in all cases, it is found that the symmetric ground state has a lower total energy than the asymmetric state (ΔE_{+UNAO} in Table S3).

Figure 5 shows the changes in electron density at a fixed lattice parameter by using the different Hubbard-corrected

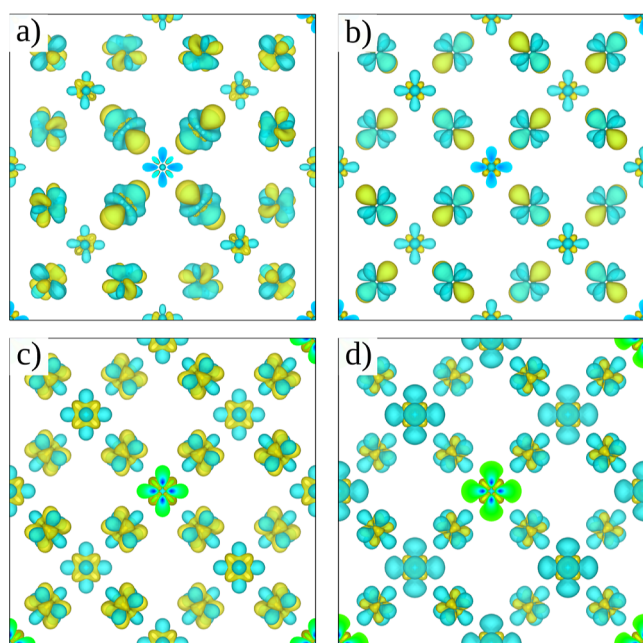


Figure 5. Electron density difference between Hubbard-corrected DFT and approximate DFT at a fixed lattice parameter. (a) DFT + U (NAO), (b) DFT + U (OAO), (c) DFT + U + V (NAO), and (d) DFT + U + V (OAO). Yellow and green colors represent the gain and loss of electron density, respectively.

theories applied in this study. First, it is interesting to note that the loss and gain of electron density from the area directly surrounding the Fe center has a δ -orbital character for all the theories. This behavior has been reported previously for other 3d transition-metal oxides⁷⁸ under DFT + U theory. In the case of DFT + U (Figure 5a,b), the loss of electron density from the region immediately around the Fe center and the increase of electron density in the regions surrounding the O atoms are observed. On the one hand, when using DFT + U -NAO, due to the loss of crystalline symmetry after the structural optimization process, it is possible to appreciate different topologies for the loss and gain of electron density around the Fe center. On the other hand, when using DFT + U -OAO, two topologies are clearly shown, which correspond

to the electron density around the Fe_{tet} and Fe_{oct} center. In the case of DFT + U + V , it is also possible to clearly identify the electron density coming from Fe_{tet} and Fe_{oct} although some interesting changes in the topology of the electron density appear. Moreover, when comparing the used projectors inside the DFT + U + V theory, it can be seen that by using OAO projectors, the loss of electron density increases.

In order to comprehend the influence of the Hubbard parameters, U and V , we can observe the action of the Hubbard potential on Kohn–Sham wave functions by obtaining the functional derivative of $E_{\text{DFT}+U+V}$ with respect to the complex conjugate of the same Kohn–Sham wave function^{13,45}

$$\hat{V}_{\text{Hub},\sigma} = \sum_I \sum_{m_1 m_2} U^I \left(\frac{\delta_{m_1 m_2}}{2} - n_{m_1 m_2}^{I\sigma} \right) \hat{p}_{m_1 m_2}^I - \sum_I \sum_{J(J \neq I)}^* \sum_{\sigma m_1 m_2} V^{IJ} n_{m_1 m_2}^{I\sigma} \hat{p}_{m_1 m_2}^I \quad (4)$$

The two components in the corrective energy functional, which are proportional to the respective on-site (U^I) and intersite (V^{IJ}) couplings, work against one another. Although the on-site term favors localization on atomic sites (usually reducing hybridization), the intersite term favors hybridized states with components on neighboring atoms. In fact, when analyzing the occupation matrices of the Hubbard-corrected approaches in Tables S3–S6, it is possible to appreciate that the potential of DFT + U theory decreases the fractional occupations regardless of the projectors used. Interestingly, the effect of the potential of the DFT + U + V theory on fractional occupations strongly depends on the projector used. When using the DFT + U + V -NAO theory, the decrease in the fractional occupations is reversed almost completely, which is not the case for DFT + U + V -OAO. This differential behavior can be explained by the fact that the V Hubbard values in DFT + U + V -NAO are bigger than for DFT + U + V -OAO.

3.5. X-ray Absorption Fine Structure Spectroscopy. X-ray absorption fine structure (XAFS) spectroscopy has become an invaluable tool for studying the electronic structure of materials. The core concept behind XAFS is based on two different regions of the measured signal: X-ray absorption near edge structure (XANES) and extended X-ray absorption fine structure (EXAFS).⁷⁹ The combination of these two types of data reveals key details about the chemical composition and overall structural properties of a sample. Then, the information derived from XAFS measurements can provide insights into bonding interactions, OS, coordination numbers, and other parameters related to the electronic properties of iron oxide materials.⁸⁰

In particular, XANES is a remarkably sensitive method for examining the valence state, ligand symmetry, coordination chemistry, and local structure close to the absorber atom. In fact, the study of magnetite has made considerable use of XANES spectroscopy over the years.^{81–86} In the XANES region, three distinctive features can be identified: the edge position ($E = E_0$), the pre-edge region ($E < E_0$), and the postedge region ($E > E_0$). Thus, we are going to analyze our simulations according to these characteristic features. Figure 6 shows the experimental and calculated Fe and O K-edge XANES spectra of Fe_3O_4 by using both uncorrected and corrected Hubbard approaches. Additionally, it can be seen from Figure S2 that disregarding the core–hole effects for the

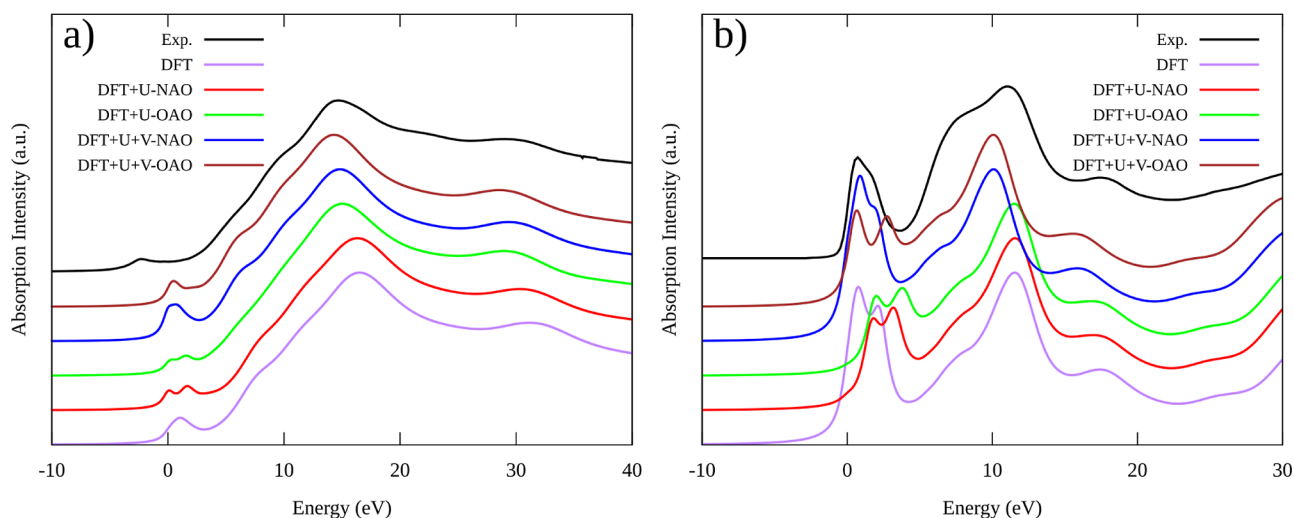


Figure 6. Simulation of Fe_3O_4 bulk (a) Fe and (b) O K-edge XANES through DFT, DFT + U , and DFT + U + V calculations using NAO and OAO projectors and comparison against respective experimental spectra (black lines).

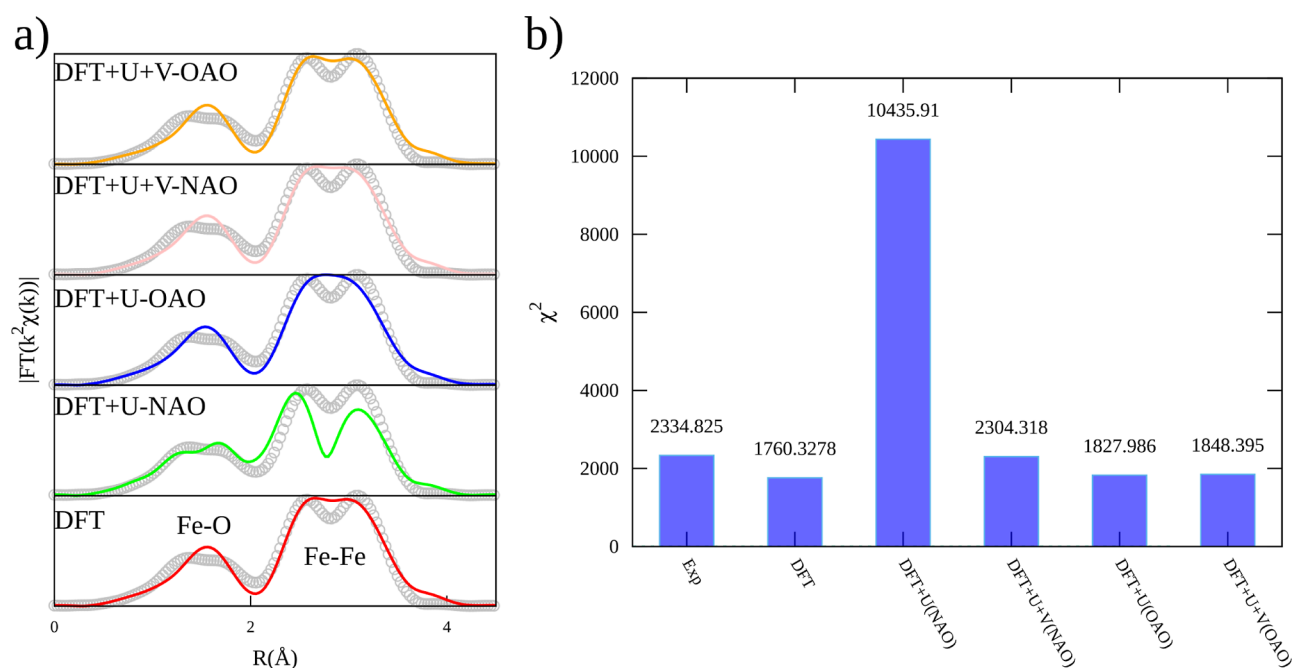


Figure 7. (a) Real part of fits (lines) of the FT signal from k^2 -weighted EXAFS signals (dots) and (b) their statistical comparison for the Fe_3O_4 bulk crystal by DFT, DFT + U , and DFT + U + V theories.

Fe K-edge in Fe_3O_4 does not significantly impact the results. This approximation is well supported for the O K-edge, but it is important to demonstrate its validity for the Fe K-edge in the context of the present study. The experimental Fe K-edge XANES spectra of Fe_3O_4 and the computed ones obtained by the theories considered in our study are compared in Figure 6a. Before getting into the specifics, it is important to note that our current experimental spectrum agrees quite well with previously published data.^{85,86} Interestingly, the simulated and experimental spectra have similar shapes. Moreover, the approximate DFT theory produces an acceptable spectrum. However, there are notable differences in the pre-edge region (0–5 eV) between the simulated and experimental spectra. Specifically, all simulated spectra show a shift toward higher energies in this region compared to the experimental spectrum. Approximate DFT values display a single broad peak in the

pre-edge region. On the contrary, implementing Hubbard correction at the DFT + U level results in a narrower double peak in this region for both NAO and the OAO projectors. Notably, DFT + U + V theory presents substantial alterations in the pre-edge compared to DFT + U . First, the pre-edge peak is simulated as a single peak for both NAO and OAO projectors. However, when employing the NAO projector to simulate the pre-edge peak, it is shown to be broader compared with that of the OAO projector. Previous studies suggest that the quadrupole-type electronic transitions between 1s and 3d orbitals and the dipole transition between 1s and 4p hybridized with 3d orbitals are responsible for the K pre-edge features.^{80,87,88} Also, due to the broken inversion symmetry in tetrahedral compounds, some p–d hybridization is possible. This means that the probability of absorption increases because of the dipole-allowed transition from the s to the p

component of the hybridized states. As a result, the intensity of the pre-edge peak is higher for tetrahedral compounds than for octahedral compounds. This is the case with magnetite (Fe_3O_4) and maghemite ($\gamma\text{-Fe}_2\text{O}_3$), where some Fe is arranged in tetrahedral coordination.⁸⁰

We now concentrate on the K-edge of Fe_3O_4 . During O K-edge X-ray absorption, the system is excited from its initial state to a final state by an X-ray with an energy of 530 eV. Herein, it is important to note that in Fe_3O_4 , each O atom has tetrahedral coordination bonded to four open-shell Fe atoms.⁸⁹ Figure 6b shows the experimental and calculations of the O 1s K-edge XANES of Fe_3O_4 . In general, there are significant similarities between the simulated and experimental spectra. However, DFT + U shows a shift to higher energies, mainly at the main edge. Even though the DFT theory simulation agrees very well with the experimental spectrum, it shows an important difference at the main edge, showing a clear splitting between 0 and 2.5 eV, which is not clear in the experimental spectrum. This splitting is also shown in the DFT + U + V-OAO spectrum with a broader extension (0–3.5 eV). The better agreement is found by using DFT + U + V-NAO, which is able to reproduce correctly the experimental pre-edge and edge characteristics.

As mentioned above, EXAFS is a powerful technique used to probe the local atomic structure, providing detailed information about the coordination environment, bond lengths, and disorder around a specific absorbing atom in a sample. The EXAFS oscillations contain valuable structural information encoded in the magnitude, phase, and frequency of the oscillations. By analyzing these oscillations, it is possible to extract the radial distribution function, which describes the distribution of neighboring atoms around the absorbing atom. Then, to ascertain the validity of each model, we compared the obtained structures to experimental EXAFS data at the Fe K-edge. The experimental data and best-fit curves for the EXAFS signal are presented in Figure 7 and Table S2. It is important to note that the same number of parameters was used in the fitting for all theories. For example, the first doublet peak in the range of 1–2 Å (which imitates the $\text{Fe}_{\text{oct}}\text{--O}$ and $\text{Fe}_{\text{tet}}\text{--O}$) was modeled by two distances of Fe–O and a single Debye–Waller factor (i.e., one order parameter). On the other hand, the second doublet peak between 2 and 4 Å (which simulates the Fe–Fe bond) has three paths corresponding to three distances and two Debye–Waller factors. For all models, the total amplitude parameter was set to a fixed value of 0.85 (following preliminary adjustment on Fe foil), while the correction to the energy scale was left open to variation. Although Figure 7a shows a close agreement between the experimental and all simulated spectra when analyzing the discrepancy between observed and expected values for the different models (7b), it is evident that DFT + U -NAO resulted in the worst experimental data adjustment. However, this model is the only one able to predict a clear splitting of the distribution in the radial range below 2 Å. This can be explained by the fact that the Fe_3O_4 structure optimization with the DFT + U -NAO theory has a charge disproportionation between Fe^{2+} and Fe^{3+} octahedral sites, which is not captured by the other models. On the contrary, the most accurate curve adjustment to the experimental data was achieved through simulation by approximate DFT and DFT + U + V (NAO and OAO projectors) methods.

According to the ligand field theory, for octahedral coordination, the 3d atomic orbitals are split into three t_{2g}

levels ($3d_{xy}$, $3d_{xz}$, and $3d_{yz}$) and two e_g levels ($3d_{x^2-y^2}$ and $3d_{z^2}$). Then, in order to get a deeper understanding of the XAS signal, we performed the orbital-projected DOS calculations under the different corrected Hubbard approaches. In Figures S2 and S3, we present the orbital projected DOS for the $3d_{xy}$, $3d_{xz}$, $3d_{yz}$, $3d_{x^2-y^2}$, and $3d_{z^2}$ orbitals for both Fe_{tet} and Fe_{oct} . However, here we will focus the discussion on Fe_{oct} due to its importance in the electronic and magnetic properties of Fe_3O_4 . In this regard, our results show that the contributions to the orbital projections to Fe_{oct} are grouped as expected, separated by t_{2g} and e_g levels. Around Fermi energy, the DFT predicted that the spin-up valence band and the spin-down conduction band overlapped practically, not presenting any discontinuity, as described previously.⁷⁵ At the DFT + U level, the spin down of Fe_{oct} has a large gap, just about t_{2g} states at Fermi energy, extending the discontinuity to the conduction band. On the contrary, at the DFT + U + V level, the gap is located just below t_{2g} states at Fermi energy. Moreover, the t_{2g} and e_g states are slightly separated at the conduction band, which is not true for the DFT + U theory. By comparing Figure 6 against Figures S2 and S3, we can conclude that the Fe K pre-edge peak originates mainly from contributions from t_{2g} spin-down orbital states of Fe_{oct} and from e and t_2 spin-up orbital states of Fe_{tet} .

Taken together, Figure 8 illustrates the energy band diagram of the Fe_{oct} 3d orbital in the Fe_3O_4 bulk crystal calculated by

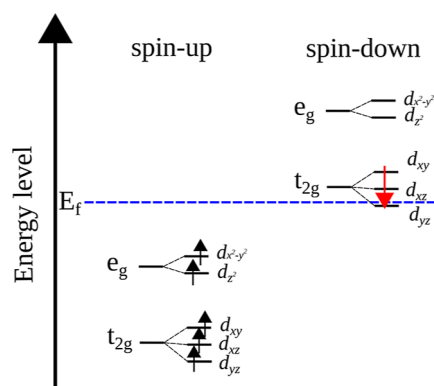


Figure 8. Energy band diagram of the Fe_{oct} 3d orbital in Fe_3O_4 bulk crystal calculated by the DFT + U + V functional.

the DFT + U + V theory. All Fe_{oct} spin-up d orbitals are occupied, while most spin-down orbitals remain unoccupied. Nonetheless, the occupation matrix and orbital-projected DOS suggest that an extra electron fractionally occupies the t_{2g} spin-down orbital of Fe_{oct} . Due to electron-sharing between Fe_{oct} sites in proximity, there are only fractional occupations of the t_{2g} spin-down orbital. This phenomenon happens because the Fe_{oct} sites share electrons with their neighboring sites and dynamically interconvert through charge hopping. As a result, these levels are not occupied completely, and their occupation matrix eigenvalues are noninteger and range from 0 to 1. Then, above T_v , the Fermi level resides in the Fe_{oct} down-spin t_{2g} band and electric conduction are 100% spin polarized, supporting the half-metallic nature of bulk crystal Fe_3O_4 .

4. CONCLUSIONS

In conclusion, using a fully first-principles approach, our study investigated the structural, magnetic, and electronic characteristics of bulk crystal Fe_3O_4 above the Verwey temperature. We

compared the results obtained from different methods, including DFT, DFT + U , DFT + U + V and HSE (hybrid functional), as well as two types of Hubbard projectors (NAO and OAO). Based on our research, we discovered that the results varied greatly depending on whether U corrections alone or both U and V corrections were employed as well as the type of Hubbard projector. The most optimal agreement was achieved through the utilization of DFT + U + V along with NAO projectors. The U parameter on-site was found to be crucial in describing the confined features of Fe 3d states while the intersite V parameter was pertinent in elucidating the robust hybridization between Fe 3d and O 2p states. While the literature often uses the same Hubbard U value for Fe_{oct} and Fe_{tet} at the DFT + U level, in this case, the HP code detected two distinct values for them through the DFT + U and DFT + U + V levels. Thus, the description of the structural, magnetic, and electronic properties of Fe₃O₄ was enhanced by the use of the extended Hubbard functional compared to standard DFT, DFT + U , and the HSE functional, without requiring excessive computational resources. Moreover, DFT + U + V validates the half-metallic character of bulk crystal Fe₃O₄ above T_v , since the Fermi level is found in the t_{2g} band with a Fe_{oct} down-spin, indicating that the electric conduction is 100% spin polarized. We believe that DFT + U + V can play a critical role in improving spectral simulations in materials science, particularly for Fe₃O₄. Therefore, our work highlights the significance of considering intersite interactions and the choice of atomic orbital projectors in future theoretical research involving Fe₃O₄ not just in its bulk form but also in its various surface and defect configurations. Also, other types of materials such as other transition-metal oxides or materials with mixed valence states could benefit from the use of DFT + U + V to accurately capture their electronic and magnetic properties and explore their potential applications.

■ ASSOCIATED CONTENT

■ Supporting Information

The Supporting Information is available free of charge at <https://pubs.acs.org/doi/10.1021/acs.jctc.3c00860>.

Calculated net charge of Fe ions, pDOS of the Fe₃O₄ bulk crystal, population analysis data, calculated energy difference, bond lengths, interatomic distances, Debye–Waller factors, eigenvalues, occupation matrices, and orbital-projected DOS, (PDF)

■ AUTHOR INFORMATION

Corresponding Author

Nelson Naveas – *Departamento de Física Aplicada, Universidad Autónoma de Madrid, 28049 Madrid, Spain; Departamento de Ingeniería Química y Procesos de Minerales, Universidad de Antofagasta, 1270300 Antofagasta, Chile; Instituto Universitario de Ciencia de Materiales “Nicolás Cabrera” (INC), Universidad Autónoma de Madrid, 28049 Madrid, Spain; orcid.org/0000-0003-0949-277X; Email: nelson.naveas@estudiante.uam.es*

Authors

Ruth Pulido – *Instituto Universitario de Ciencia de Materiales “Nicolás Cabrera” (INC), Universidad Autónoma de Madrid, 28049 Madrid, Spain; Departamento de Química, Universidad de Antofagasta, 1270300 Antofagasta, Chile*

Carlo Marini – *CELLS–ALBA Synchrotron, 08290*

Cerdanyola del Valles, Spain

Pierluigi Gargiani – *CELLS–ALBA Synchrotron, 08290*

Cerdanyola del Valles, Spain; orcid.org/0000-0002-6649-0538

Jacobo Hernandez-Montelongo – *Departamento de Ciencias Matemáticas y Físicas, UC Temuco, 4813302 Temuco, Chile*

Ivan Brito – *Departamento de Química, Universidad de Antofagasta, 1270300 Antofagasta, Chile; orcid.org/0000-0001-6077-2457*

Miguel Manso-Silván – *Departamento de Física Aplicada, Universidad Autónoma de Madrid, 28049 Madrid, Spain; Instituto Universitario de Ciencia de Materiales “Nicolás Cabrera” (INC) and Centro de Microanálisis de Materiales, Universidad Autónoma de Madrid, 28049 Madrid, Spain; orcid.org/0000-0002-5063-1607*

Complete contact information is available at:

<https://pubs.acs.org/doi/10.1021/acs.jctc.3c00860>

■ Author Contributions

Conceptualization, N.N.; theoretical calculations, N.N. and R.P.; experimental and simulation XAS analysis, N.N., M.M.-S., P.G., and C.M.; computational simulations, N.N., I.B., J.H.-M., and C.M.; writing—original draft preparation, N.N. and R.P.; and project application, M.M.-S. All authors have read and agreed to the published version of the manuscript.

■ Notes

The authors declare no competing financial interest.

■ ACKNOWLEDGMENTS

We recognize to PhD. Programs in “Advanced Materials and Nanotechnologies” from Universidad Autónoma de Madrid (UAM, Spain) and “Ingeniería de Procesos de Minerales” from Universidad de Antofagasta (UA, Chile). This work was financially supported by CONICYT PFCHA/DOCTORADO/2017-21172001 (Nelson Naveas) and partially funded by Project USAMPSA, PID-2020-112770-C22, from the Government of Spain. Moreover, we acknowledge the ALBA synchrotron facility for beamtime no. 2020024325 at the CLÆSS beamline. The simulations used in this paper have been performed in the Centro de Computación Científica-Universidad Autónoma de Madrid (CCC-UAM); thanks to CPU time and other resources granted by the institution.

■ REFERENCES

- (1) Hohenberg, P.; Kohn, W. Inhomogeneous Electron Gas. *Phys. Rev.* **1964**, *136*, B864–B871.
- (2) Kohn, W.; Sham, L. J. Self-Consistent Equations Including Exchange and Correlation Effects. *Phys. Rev.* **1965**, *140*, A1133–A1138.
- (3) Becke, A. D. Perspective: Fifty years of density-functional theory in chemical physics. *J. Chem. Phys.* **2014**, *140*, 18A301.
- (4) Meng, Y.; Liu, X.-W.; Huo, C.-F.; Guo, W.-P.; Cao, D.-B.; Peng, Q.; Dearden, A.; Gonze, X.; Yang, Y.; Wang, J.; Jiao, H.; Li, Y.; Wen, X.-D. When Density Functional Approximations Meet Iron Oxides. *J. Chem. Theory Comput.* **2016**, *12*, 5132–5144.
- (5) Mori-Sánchez, P.; Cohen, A. J.; Yang, W. Many-electron self-interaction error in approximate density functionals. *J. Chem. Phys.* **2006**, *125*, 201102.
- (6) Cramer, C. J.; Truhlar, D. G. Density functional theory for transition metals and transition metal chemistry. *Phys. Chem. Chem. Phys.* **2009**, *11*, 10757–10816.
- (7) Jiang, H.; Gomez-Abal, R. I.; Rinke, P.; Scheffler, M. First-principles modeling of localized d states with the GW @LDA + U

- approach. *Phys. Rev. B: Condens. Matter Mater. Phys.* **2010**, *82*, 045108.
- (8) Janesko, B. G. Replacing hybrid density functional theory: motivation and recent advances. *Chem. Soc. Rev.* **2021**, *50*, 8470–8495.
- (9) Kirchner-Hall, N. E.; Zhao, W.; Xiong, Y.; Timrov, I.; Dabo, I. Extensive Benchmarking of DFT+U Calculations for Predicting Band Gaps. *Appl. Sci.* **2021**, *11*, 2395.
- (10) Anisimov, V. I.; Poteryaev, A. I.; Korotin, M. A.; Anokhin, A. O.; Kotliar, G. First-principles calculations of the electronic structure and spectra of strongly correlated systems: dynamical mean-field theory. *J. Phys.: Condens. Matter* **1997**, *9*, 7359–7367.
- (11) Dudarev, S. L.; Botton, G. A.; Savrasov, S. Y.; Humphreys, C. J.; Sutton, A. P. Electron-energy-loss spectra and the structural stability of nickel oxide: An LSDA+U study. *Phys. Rev. B: Condens. Matter Mater. Phys.* **1998**, *57*, 1505–1509.
- (12) Himmetoglu, B.; Floris, A.; de Gironcoli, S.; Cococcioni, M. Hubbard-corrected DFT energy functionals: The LDA+U description of correlated systems. *Int. J. Quantum Chem.* **2014**, *114*, 14–49.
- (13) Leiria Campo, V.; Cococcioni, M. Extended DFT + U + V method with on-site and inter-site electronic interactions. *J. Phys.: Condens. Matter* **2010**, *22*, 055602.
- (14) Santos-Carballal, D.; Roldan, A.; Grau-Crespo, R.; de Leeuw, N. H. A DFT study of the structures, stabilities and redox behaviour of the major surfaces of magnetite Fe_3O_4 . *Phys. Chem. Chem. Phys.* **2014**, *16*, 21082–21097.
- (15) Liu, H.; Di Valentin, C. Bulk-terminated or reconstructed $\text{Fe}_3\text{O}_4(001)$ surface: water makes a difference. *Nanoscale* **2018**, *10*, 11021–11027.
- (16) Yu, M.; Yang, S.; Wu, C.; Marom, N. Machine learning the Hubbard U parameter in DFT+U using Bayesian optimization. *npj Comput. Mater.* **2020**, *6*, 180.
- (17) Pulido, R.; Naveas, N.; Jmartín-Palma, R.; Graber, T.; Brito, I.; Hernández-Montelongo, J.; Manso Silván, M. Experimental and density functional theory study of the Li^+ desorption in spinel/layered lithium manganese oxide nanocomposites using HCl. *Chem. Eng. J.* **2022**, *441*, 136019.
- (18) Dederichs, P. H.; Blügel, S.; Zeller, R.; Akai, H. Ground States of Constrained Systems: Application to Cerium Impurities. *Phys. Rev. Lett.* **1984**, *53*, 2512–2515.
- (19) McMahan, A. K.; Martin, R. M.; Satpathy, S. Calculated effective Hamiltonian for La_2CuO_4 and solution in the impurity Anderson approximation. *Phys. Rev. B: Condens. Matter Mater. Phys.* **1988**, *38*, 6650–6666.
- (20) Gunnarsson, O.; Andersen, O. K.; Jepsen, O.; Zaanen, J. Density-functional calculation of the parameters in the Anderson model: Application to Mn in CdTe. *Phys. Rev. B: Condens. Matter Mater. Phys.* **1989**, *39*, 1708–1722.
- (21) Hybertsen, M. S.; Schlüter, M.; Christensen, N. E. Calculation of Coulomb-interaction parameters for La_2CuO_4 using a constrained-density-functional approach. *Phys. Rev. B: Condens. Matter Mater. Phys.* **1989**, *39*, 9028–9041.
- (22) Gunnarsson, O. Calculation of parameters in model Hamiltonians. *Phys. Rev. B: Condens. Matter Mater. Phys.* **1990**, *41*, 514–518.
- (23) Pickett, W. E.; Erwin, S. C.; Ethridge, E. C. Reformulation of the LDA + U method for a local-orbital basis. *Phys. Rev. B: Condens. Matter Mater. Phys.* **1998**, *58*, 1201–1209.
- (24) Solovyev, I. V.; Imada, M. Screening of Coulomb interactions in transition metals. *Phys. Rev. B: Condens. Matter Mater. Phys.* **2005**, *71*, 045103.
- (25) Nakamura, K.; Arita, R.; Yoshimoto, Y.; Tsuneyuki, S. First-principles calculation of effective onsite Coulomb interactions of 3d transition metals: Constrained local density functional approach with maximally localized Wannier functions. *Phys. Rev. B: Condens. Matter Mater. Phys.* **2006**, *74*, 235113.
- (26) Mosey, N. J.; Carter, E. A. Ab initio evaluation of Coulomb and exchange parameters for DFT + U calculations. *Phys. Rev. B: Condens. Matter Mater. Phys.* **2007**, *76*, 155123.
- (27) Mosey, N. J.; Liao, P.; Carter, E. A. Rotationally invariant ab initio evaluation of Coulomb and exchange parameters for DFT+U calculations. *J. Chem. Phys.* **2008**, *129*, 014103.
- (28) Andriotis, A. N.; Sheetz, R. M.; Menon, M. LSDA + U method: A calculation of the U values at the Hartree-Fock level of approximation. *Phys. Rev. B: Condens. Matter Mater. Phys.* **2010**, *81*, 245103.
- (29) Agapito, L. A.; Curtarolo, S.; Buongiorno Nardelli, M. Reformulation of DFT + U as a Pseudohybrid Hubbard Density Functional for Accelerated Materials Discovery. *Phys. Rev. X* **2015**, *5*, 011006.
- (30) Tancogne-Dejean, N.; Rubio, A. Parameter-free hybridlike functional based on an extended Hubbard model: DFT + U + V. *Phys. Rev. B* **2020**, *102*, 155117.
- (31) Lee, S.-H.; Son, Y.-W. First-principles approach with a pseudohybrid density functional for extended Hubbard interactions. *Phys. Rev. Res.* **2020**, *2*, 043410.
- (32) Springer, M.; Aryasetiawan, F. Frequency-dependent screened interaction in Ni within the random-phase approximation. *Phys. Rev. B: Condens. Matter Mater. Phys.* **1998**, *57*, 4364–4368.
- (33) Kotani, T. Ab initio random-phase-approximation calculation of the frequency-dependent effective interaction between 3d electrons: Ni, Fe, and MnO. *J. Phys.: Condens. Matter* **2000**, *12*, 2413–2422.
- (34) Aryasetiawan, F.; Imada, M.; Georges, A.; Kotliar, G.; Biermann, S.; Lichtenstein, A. I. Frequency-dependent local interactions and low-energy effective models from electronic structure calculations. *Phys. Rev. B: Condens. Matter Mater. Phys.* **2004**, *70*, 195104.
- (35) Aryasetiawan, F.; Karlsson, K.; Jepsen, O.; Schönberger, U. Calculations of Hubbard U from first-principles. *Phys. Rev. B: Condens. Matter Mater. Phys.* **2006**, *74*, 125106.
- (36) Vaugier, L.; Jiang, H.; Biermann, S. Hubbard U and Hund exchange J in transition metal oxides: Screening versus localization trends from constrained random phase approximation. *Phys. Rev. B: Condens. Matter Mater. Phys.* **2012**, *86*, 165105.
- (37) Amadon, B.; Applencourt, T.; Bruneval, F. Screened Coulomb interaction calculations: cRPA implementation and applications to dynamical screening and self-consistency in uranium dioxide and cerium. *Phys. Rev. B: Condens. Matter Mater. Phys.* **2014**, *89*, 125110.
- (38) Timrov, I.; Marzari, N.; Cococcioni, M. Hubbard parameters from density-functional perturbation theory. *Phys. Rev. B* **2018**, *98*, 085127.
- (39) Timrov, I.; Marzari, N.; Cococcioni, M. Self-consistent Hubbard parameters from density-functional perturbation theory in the ultrasoft and projector-augmented wave formulations. *Phys. Rev. B* **2021**, *103*, 045141.
- (40) Walz, F. The Verwey transition - a topical review. *J. Phys.: Condens. Matter* **2002**, *14*, R285–R340.
- (41) Verwey, E. J. W. Electronic Conduction of Magnetite (Fe_3O_4) and its Transition Point at Low Temperatures. *Nature* **1939**, *144*, 327–328.
- (42) Attfield, J. Magnetism and the Trimeron Bond. *Chem. Mater.* **2022**, *34*, 2877–2885.
- (43) Giannozzi, P.; Baroni, S.; Bonini, N.; Calandra, M.; Car, R.; Cavazzoni, C.; Ceresoli, D.; Chiarotti, G. L.; Cococcioni, M.; Dabo, I.; Dal Corso, A.; de Gironcoli, S.; Fabris, S.; Fratesi, G.; Gebauer, R.; Gerstmann, U.; Gougoussis, C.; Kokalj, A.; Lazzeri, M.; Martin-Samos, L.; Marzari, N.; Mauri, F.; Mazzarello, R.; Paolini, S.; Pasquarello, A.; Paulatto, L.; Sbraccia, C.; Scandolo, S.; Sclauzero, G.; Seitsonen, A. P.; Smogunov, A.; Umari, P.; Wentzcovitch, R. M. Quantum Espresso: a modular and open-source software project for quantum simulations of materials. *J. Phys.: Condens. Matter* **2009**, *21*, 395502.
- (44) Prandini, G.; Marrazzo, A.; Castelli, I. E.; Mounet, N.; Marzari, N. Precision and efficiency in solid-state pseudopotential calculations. *npj Comput. Mater.* **2018**, *4*, 72.
- (45) Timrov, I.; Marzari, N.; Cococcioni, M. HP – A code for the calculation of Hubbard parameters using density-functional perturbation theory. *Comput. Phys. Commun.* **2022**, *279*, 108455.

- (46) Cococcioni, M.; de Gironcoli, S. Linear response approach to the calculation of the effective interaction parameters in the LDA + U method. *Phys. Rev. B: Condens. Matter Mater. Phys.* **2005**, *71*, 035105.
- (47) Marzari, N.; Vanderbilt, D.; De Vita, A.; Payne, M. C. Thermal Contraction and Disordering of the Al(110) Surface. *Phys. Rev. Lett.* **1999**, *82*, 3296–3299.
- (48) Henkelman, G.; Arnaldsson, A.; Jónsson, H. A fast and robust algorithm for Bader decomposition of charge density. *Comput. Mater. Sci.* **2006**, *36*, 354–360.
- (49) Sanville, E.; Kenny, S. D.; Smith, R.; Henkelman, G. Improved grid-based algorithm for Bader charge allocation. *J. Comput. Chem.* **2007**, *28*, 899–908.
- (50) Tang, W.; Sanville, E.; Henkelman, G. A grid-based Bader analysis algorithm without lattice bias. *J. Phys.: Condens. Matter* **2009**, *21*, 084204.
- (51) Yu, M.; Trinkle, D. R. Accurate and efficient algorithm for Bader charge integration. *J. Chem. Phys.* **2011**, *134*, 064111.
- (52) Taillefumier, M.; Cabaret, D.; Flank, A.-M.; Mauri, F. X-ray absorption near-edge structure calculations with the pseudopotentials: Application to the K edge in diamond and α -quartz. *Phys. Rev. B: Condens. Matter Mater. Phys.* **2002**, *66*, 195107.
- (53) Gougousis, C.; Calandra, M.; Seitsonen, A.; Brouder, C.; Shukla, A.; Mauri, F. Intrinsic charge transfer gap in NiO from Ni K-edge x-ray absorption spectroscopy. *Phys. Rev. B: Condens. Matter Mater. Phys.* **2009**, *79*, 045118.
- (54) Timrov, I.; Agrawal, P.; Zhang, X.; Erat, S.; Liu, R.; Braun, A.; Cococcioni, M.; Calandra, M.; Marzari, N.; Passerone, D. Electronic structure of pristine and Ni-substituted LaFeO₃ from near edge x-ray absorption fine structure experiments and first-principles simulations. *Phys. Rev. Res.* **2020**, *2*, 033265.
- (55) Bunău, O.; Calandra, M. Projector augmented wave calculation of x-ray absorption spectra at the $L_{2,3}$ edges. *Phys. Rev. B: Condens. Matter Mater. Phys.* **2013**, *87*, 205105.
- (56) Paris, E.; Simonelli, L.; Wakita, T.; Marini, C.; Lee, J.-H.; Olszewski, W.; Terashima, K.; Kakuto, T.; Nishimoto, N.; Kimura, T.; Kudo, K.; Kambe, T.; Nohara, M.; Yokoya, T.; Saini, N. Temperature dependent local atomic displacements in ammonia intercalated iron selenide superconductor. *Sci. Rep.* **2016**, *6*, 27646.
- (57) Rehr, J. J.; Albers, R. C. Theoretical approaches to x-ray absorption fine structure. *Rev. Mod. Phys.* **2000**, *72*, 621–654.
- (58) Ravel, B.; Newville, M. ATHENA, ARTEMIS, HEPHAESTUS: data analysis for X-ray absorption spectroscopy using IFEFFIT. *J. Synchrotron Radiat.* **2005**, *12*, 537–541.
- (59) Aschauer, U.; Selloni, A. Adsorption of biomedical coating molecules, amino acids, and short peptides on magnetite (110). *J. Chem. Phys.* **2015**, *143*, 044705.
- (60) Kulik, H. J.; Marzari, N. A self-consistent Hubbard U density-functional theory approach to the addition-elimination reactions of hydrocarbons on bare FeO+. *J. Chem. Phys.* **2008**, *129*, 66.
- (61) Shishkin, M.; Sato, H. Self-consistent parametrization of DFT + U framework using linear response approach: Application to evaluation of redox potentials of battery cathodes. *Phys. Rev. B* **2016**, *93*, 085135.
- (62) Naveas, N.; Pulido, R.; Marini, C.; Hernández-Montelongo, J.; Silván, M. M. First-principles calculations of hematite (α -Fe₂O₃) by self-consistent DFT+U+V. *iScience* **2023**, *26*, 106033.
- (63) Ricca, C.; Timrov, I.; Cococcioni, M.; Marzari, N.; Aschauer, U. Self-consistent DFT + U + V study of oxygen vacancies in SrTiO₃. *Phys. Rev. Res.* **2020**, *2*, 023313.
- (64) Mahajan, R.; Kashyap, A.; Timrov, I. Pivotal Role of Intersite Hubbard Interactions in Fe-Doped α -MnO₂. *J. Phys. Chem. C* **2022**, *126*, 14353–14365.
- (65) Wright, J. P.; Attfield, J. P.; Radaelli, P. G. Charge ordered structure of magnetite Fe₃O₄ below the Verwey transition. *Phys. Rev. B: Condens. Matter Mater. Phys.* **2002**, *66*, 214422.
- (66) Parkinson, G. S. Iron oxide surfaces. *Surf. Sci. Rep.* **2016**, *71*, 272–365.
- (67) Goering, E.; Gold, S.; Lafkoti, M.; Schütz, G. Vanishing Fe 3d orbital moments in single-crystalline magnetite. *Europhys. Lett.* **2006**, *73*, 97–103.
- (68) Rakhecha, V. C.; Murthy, N. S. Spin-transfer due to covalency for the tetrahedral-site Fe³⁺ ions in Fe₃O₄. *J. Phys. C: Solid State Phys.* **1978**, *11*, 4389–4404.
- (69) Sit, P.; Car, R.; Cohen, M.; Selloni, A. Simple, Unambiguous Theoretical Approach to Oxidation State Determination via First-Principles Calculations. *Inorg. Chem.* **2011**, *50*, 10259–10267.
- (70) Dedkov, Y.; Fonin, M.; Vyalikh, D.; Hauch, J.; Molodtsov, S.; Rüdiger, U.; Güntherodt, G. Electronic structure of the Fe₃O₄(111) surface. *Phys. Rev. B: Condens. Matter Mater. Phys.* **2004**, *70*, 073405.
- (71) Park, S. K.; Ishikawa, T.; Tokura, Y. Charge-gap formation upon the Verwey transition in Fe₃O₄. *Phys. Rev. B: Condens. Matter Mater. Phys.* **1998**, *58*, 3717–3720.
- (72) Park, J.-H.; Tjeng, L. H.; Allen, J. W.; Metcalf, P.; Chen, C. T. Single-particle gap above the Verwey transition in Fe₃O₄. *Phys. Rev. B: Condens. Matter Mater. Phys.* **1997**, *55*, 12813–12817.
- (73) Chainani, A.; Yokoya, T.; Morimoto, T.; Takahashi, T.; Todo, S. High-resolution photoemission spectroscopy of the Verwey transition in Fe₃O₄. *Phys. Rev. B: Condens. Matter Mater. Phys.* **1995**, *51*, 17976–17979.
- (74) Zhang, Z.; Satpathy, S. Electron states, magnetism, and the Verwey transition in magnetite. *Phys. Rev. B: Condens. Matter Mater. Phys.* **1991**, *44*, 13319–13331.
- (75) Noh, J.; Osman, O. I.; Aziz, S. G.; Winget, P.; Brédas, J. L. A density functional theory investigation of the electronic structure and spin moments of magnetite. *Sci. Technol. Adv. Mater.* **2014**, *15*, 044202.
- (76) Liu, H.; Di Valentin, C. Band Gap in Magnetite Above Verwey Temperature Induced by Symmetry Breaking. *J. Phys. Chem. C* **2017**, *121*, 25736–25742.
- (77) Rowan, A. D.; Patterson, C. H.; Gasparov, L. V. Hybrid density functional theory applied to magnetite: Crystal structure, charge order, and phonons. *Phys. Rev. B: Condens. Matter Mater. Phys.* **2009**, *79*, 205103.
- (78) Zhao, Q.; Kulik, H. J. Where Does the Density Localize in the Solid State? Divergent Behavior for Hybrids and DFT+U. *J. Chem. Theory Comput.* **2018**, *14*, 670–683.
- (79) Fornasini, P. In *Synchrotron Radiation: Basics, Methods and Applications*; Mobilio, S.; Boscherini, F.; Meneghini, C., Eds.; Springer Berlin Heidelberg: Berlin, Heidelberg, 2015; pp 181–211.
- (80) Fdez-Gubieda, M. L.; García-Prieto, A.; Alonso, J.; Meneghini, C. *Iron Oxides*; John Wiley & Sons, Ltd, 2016; Chapter 17, pp 397–422.
- (81) O'Day, P. A.; Rivera, N.; Root, R.; Carroll, S. A.; Carroll, S. A. X-ray absorption spectroscopic study of Fe reference compounds for the analysis of natural sediments. *Am. Mineral.* **2004**, *89*, 572–585.
- (82) Larumbe, S.; Gomez-Polo, C.; Pérez-Landazábal, J. I.; García-Prieto, A.; Alonso, J.; Fdez-Gubieda, M. L.; Cordero, D.; Gómez, J. Ni doped Fe₃O₄ magnetic nanoparticles. *J. Nanosci. Nanotechnol.* **2012**, *12*, 2652–2660.
- (83) Okudera, H.; Yoshiasa, A.; Murai, K. i.; Okube, M.; Takeda, T.; Kikkawa, S. Local structure of magnetite and maghemite and chemical shift in Fe K-edge XANES. *J. Mineral. Petrol. Sci.* **2012**, *107*, 127–132.
- (84) Espinosa, A.; Serrano, A.; Llavona, A.; Jiménez de la Morena, J.; Abuin, M.; Figuerola, A.; Pellegrino, T.; Fernández, J. F.; García-Hernández, M.; Castro, G. R.; García, M. A. On the discrimination between magnetite and maghemite by XANES measurements in fluorescence mode. *Meas. Sci. Technol.* **2011**, *23*, 015602.
- (85) Espinosa, A.; Muñoz-Noval, A.; García-Hernández, M.; Serrano, A.; Jiménez de la Morena, J.; Figuerola, A.; Quarta, A.; Pellegrino, T.; Wilhelm, C.; García, M. A. Magnetic properties of iron oxide nanoparticles prepared by seeded-growth route. *J. Nanopart. Res.* **2013**, *15*, 1514.
- (86) Piquer, C.; Laguna-Marco, M.; Roca, A. G.; Boada, R.; Guglieri, C.; Chaboy, J. Fe K-Edge X-ray Absorption Spectroscopy Study of Nanosized Nominal Magnetite. *J. Phys. Chem. C* **2014**, *118*, 1332–1346.

- (87) Henderson, G. S.; de Groot, F. M.; Moulton, B. J. X-ray Absorption Near-Edge Structure (XANES) Spectroscopy. *Rev. Mineral. Geochem.* **2014**, *78*, 75–138.
- (88) Pascarelli, S. In *Synchrotron Radiation: Basics, Methods and Applications*; Mobilio, S., Boscherini, F., Meneghini, C., Eds.; Springer Berlin Heidelberg: Berlin, Heidelberg, 2015; pp 737–760.
- (89) Sassi, M.; Pearce, C.; Bagus, P.; Arenholz, E.; Rosso, K. First Principles Fe $L_{2,3}$ -Edge and O K-Edge XANES and XMCD Spectra for Iron Oxides. *J. Phys. Chem. A* **2017**, *121*, 7613–7618.